

BolT: Fused Window Transformers for fMRI Time Series Analysis

Hasan Atakan Bedel Irmak Şıvgın Onat Dalmaz Salman UI Hassan Dar Tolga Çukur

Department of Electrical and Electronics Engineering

Bilkent University

Ankara, Turkey

atakan.bedelee@gmail.com, cukur@ee.bilkent.edu.tr

Abstract

Functional magnetic resonance imaging (fMRI) enables examination of inter-regional interactions in the brain via functional connectivity (FC) analyses that measure the synchrony between the temporal activations of separate regions. Given their exceptional sensitivity, deep-learning methods have received growing interest for FC analyses of high-dimensional fMRI data. In this domain, models that operate directly on raw time series as opposed to pre-computed FC features have the potential benefit of leveraging the full scale of information present in fMRI data. However, previous models are based on architectures suboptimal for temporal integration of representations across multiple time scales. Here, we present BolT, blood-oxygen-level-dependent transformer, for analyzing multi-variate fMRI time series. BolT leverages a cascade of transformer encoders equipped with a novel fused window attention mechanism. Transformer encoding is performed on temporally-overlapped time windows within the fMRI time series to capture short time-scale representations. To integrate information across windows, cross-window attention is computed between base tokens in each time window and fringe tokens from neighboring time windows. To transition from local to global representations, the extent of window overlap and thereby number of fringe tokens is progressively increased across the cascade. Finally, a novel cross-window regularization is enforced to align the high-level representations of global *CLS* features across time windows. Comprehensive experiments on public fMRI datasets clearly illustrate the superior performance of BolT against state-of-the-art methods. Posthoc explanatory analyses to identify landmark time points and regions that contribute most significantly to model decisions corroborate prominent neuroscientific findings from recent fMRI studies. Code for implementing BolT will be publicly available at <https://github.com/icon-lab/BolT>.

1 Introduction

Functional magnetic resonance imaging (fMRI) is a neuroimaging modality that non-invasively monitors cortical responses via blood-oxygen-level-dependent (BOLD) signals [45]. BOLD signals characteristically reflect changes in metabolic demand consequent to neural activity during cognitive tasks [33, 22, 36, 26]. By recording these signals with an unparalleled combination of spatio-temporal resolution and coverage, fMRI enables multi-variate analysis of functional interactions across the meticulous hierarchy of brain regions. Because the human brain mediates cognitive tasks via information processing across this hierarchy, multi-variate analyses of fMRI data helps advance our understanding of brain function in normal and disease states [18, 41, 8, 10].

The traditional fMRI approach to examine multi-variate interactions across brain regions is to extract functional connectivity (FC) features, typically taken as the correlation between the respective BOLD time series [20, 43]. The distribution of FC features across the brain can then be analyzed to identify associations with behavioral traits, or prominent neurological diseases [23, 9, 6, 2]. Given the capability of deep learning in capturing complex patterns in data, there has been a growing interest in deep-learning based analysis of FC features in cortical networks [29, 32, 3, 30, 34]. A common approach in this domain is based on convolutional or graphical models that map pre-extracted FC features to task variables or disease state [39, 21, 34, 31]. Despite their efficiency, models that receive FC features as primary input potentially ignore the non-linear interactions among brain regions evident in raw BOLD time series. To more directly assess information in BOLD signals, several recent studies have instead built classifiers based on either recurrent models or hybrid Convolutional Neural Network (CNN)-Transformer models for spatio-temporal encoding [17, 38, 37]. Hybrid architectures operating on voxel-level inputs are computationally demanding due to the dimensionality of fMRI data, and previously proposed recurrent and hybrid architectures do not possess explicit mechanisms for capturing brain activation dynamics spanning across diverse time scales [28].

Here we propose a novel BOLD transformer architecture, BolT, for fMRI time-series classification. To capture local representations at short time scales, transformer blocks in BolT encode temporally overlapping windows within fMRI times series. Unlike previous transformer models, BolT leverages a novel fused window attention mechanism to enhance expressiveness for representations across a broad range of time scales. In particular, cross-window attention is computed between base BOLD tokens in each time window and fringe tokens from neighboring time windows. The extent of window overlap and thereby fringe tokens is progressively increased across the cascade to capture a hierarchy of global representations. Finally, a novel cross-window regularization is enforced to align the high-level representations of global *CLS* features across time windows. BolT mitigates computational burden by processing ROI-wise raw BOLD signals, and by employing a fused window mechanism that scales linearly with the temporal length of the fMRI scan.

We demonstrate BolT on two large-scale public fMRI datasets: for gender classification and task decoding in the Human Connectome Project (HCP) dataset [50] and disease detection in the Autism Brain Imaging Data Exchange (ABIDE) dataset [15]. Our results indicate state-of-the-art performance compared to prior traditional and deep-learning methods, including recent transformer baselines. To interpret the representational information captured by BolT, we adopt a powerful explanatory approach [7] on our fused-window attention operators and construct relevancy maps to identify landmark time points that most significantly contribute to the model’s decision. Importantly, these landmark points closely match the task timings in task-based fMRI scans. Furthermore, via a logistic regression model fit on brain activations retrieved from landmark points, we identify target brain sites for gender classification and disease detection from resting-state fMRI scans. Our model reveals a host of target sites that corroborate the neuroscientific findings from recent large-scale fMRI studies.

2 Related work

Following their mainstream utilization in language tasks [51, 14, 40, 4], transformers have also started to powerhouse many state-of-the-art models in vision tasks [16, 25, 35, 52]. Inspired by this success, few recent studies [31, 53, 38, 37, 53] have adopted transformer-based architectures for analysis of fMRI data. In [31], the STAGIN method was proposed that incorporates a single-head transformer encoder to a graphical neural network (GNN) model for improving temporal explainability. The transformer encoder in STAGIN processes the temporal sequence of graphical features derived by the GNN based on from dynamic FC features as input. Higher gender classification accuracy was reported on resting-state fMRI data with the added transformer in STAGIN. In [53], a pair of vanilla transformers [51] was used on task-based fMRI to extract the temporal and spatial features of volumetric fMRI data respectively. Following self-supervised pretraining, subject-specific brain networks were analyzed based on extracted feature sets. With closer aims to our study, BAnD first uses 3D CNNs to extract spatial features of volumetric fMRI data, followed by a two-layer vanilla transformer with a *CLS* token for task classification in task-based fMRI [38]. Yet, BAnD allows for only fixed-length sequences with absolute position encoding, limiting flexibility for experimental designs of varying duration. Furthermore, BAnD’s transformer processes the entire fMRI time series as a single sequence, focusing on global representations at the expense of local precision. Following a similar approach to BAnD, TFF also uses a 3D CNN to derive spatial features of volumetric fMRI

data, albeit it uses a transformer encoder to process short sequences of the fMRI time series as separate time windows [37]. Because TFF processes each time window independently, it focuses on local representations and therefore it can miss long-range temporal relations in fMRI data. Note that both BAnD and TFF involve cascaded 3D CNN and transformer blocks that elevate overall model complexity, and necessitate pre-training on large datasets for reliable performance [38, 37].

To sensitively examine the broad scale of inter-regional interactions across time while mitigating computational burden, here we introduce a novel transformer architecture based on a fused window self-attention mechanism, BolT. Unlike traditional and learning-based methods that receive as input pre-extracted FC features [1, 39, 21, 34, 31], BolT performs learning directly on raw BOLD signals to maximize expressiveness for intricate information in fMRI scans. Unlike recent efforts that process voxel-level BOLD signals with the aid of CNNs [37, 38], BolT accepts ROI-wise BOLD signals to mitigate computational burden, and directly processes these BOLD signals with a cascaded transformer encoder. Perhaps, the closest to our work is TFF [37] that analyzes CNN-extracted spatial features of fMRI data in short time segments. However, unlike TFF that performs blind averaging of transformer-encoded feature maps across separate time windows, BolT introduces a novel fused window multi-head self-attention layer (FW-MSA, Section 3.1). FW-MSA captures inter-regional relationships that extend over broad time scales via learning-based fusion of information flow across separate time windows. Of high practical relevance, our proposed model does not require any pre-training procedures as it can be trained from scratch to encode ROI-level BOLD signals according to a public brain atlas. As such, it enables an order of magnitude improvement in training and inference times compared to voxel-level transformer models as reported in [37, 38].

3 Methods

For multi-variate analysis of fMRI time series, regional BOLD signals are first extracted from 4D fMRI data using an external atlas parcellating the brain into N regions-of-interest (ROIs). The BOLD time series for a given ROI is taken as the average signal across voxels within the ROI, and the resultant time series is z-scored to zero mean and unit variance. Our transformer model learns to map these regional BOLD signals onto class labels (e.g. subject gender, cognitive task) depending on the classification task. Note that transformers expect a sequence of tokens as input. Here, we refer to the collection of BOLD signals across the brain measured at a particular time index as a BOLD token. The BOLD token at time index t is denoted as $b^{(t)} \in \mathbb{R}^N$, the collection of BOLD tokens in a given subject across the fMRI scan is denoted as $x_{subject} = (b^{(0)}, \dots, b^{(T-1)})$ where $x_{subject} \in \mathbb{R}^{N \times T}$ and T is the scan duration. Latent representations of BOLD tokens for a given scan are computed by a cascade of BolT transformer blocks (Figure 1). The learned latent feature h_f is then linearly projected onto individual class probabilities. To capture both local and global representations of BOLD tokens, the transformer blocks in BolT split the fMRI time series into M overlapping windows, and employ a novel fused window self-attention operator to assess interactions between base tokens in a given time window and fringe tokens in neighboring windows. In the rest of this section, we describe the technical details of the BolT architecture, describe explainability analyses, datasets and experimental settings under which BolT has been demonstrated.

3.1 BolT

BolT embodies a serial cascade of transformer blocks and a final linear layer to perform classification. Unlike a vanilla transformer [51], BolT comprises a novel fused windowed multi-head self-attention (FW-MSA) layer to enhance sensitivity to the diverse time scales of dynamic interactions in the brain, while maintaining linear scalability with the duration of fMRI scans (Figure 2). Unlike vanilla MSA that computes global attention with quadratic complexity, FW-MSA computes local attention within compact time windows extracted from the fMRI time series. Temporal windowing restricts token-to-token interactions to a focal neighborhood surrounding each window. The resultant local precision serves to improve capture of subtle changes in brain activation dynamics. To capture a window-level latent representation, a *CLS* token is also employed for use in classification tasks [14, 16]. Input *CLS* tokens are initialized as tied vectors across separate time windows. The *CLS* token for each window is concatenated to the query, value and key tokens in FW-MSA. The final layer uses output *CLS* tokens to linear map their aggregate features onto class logits.

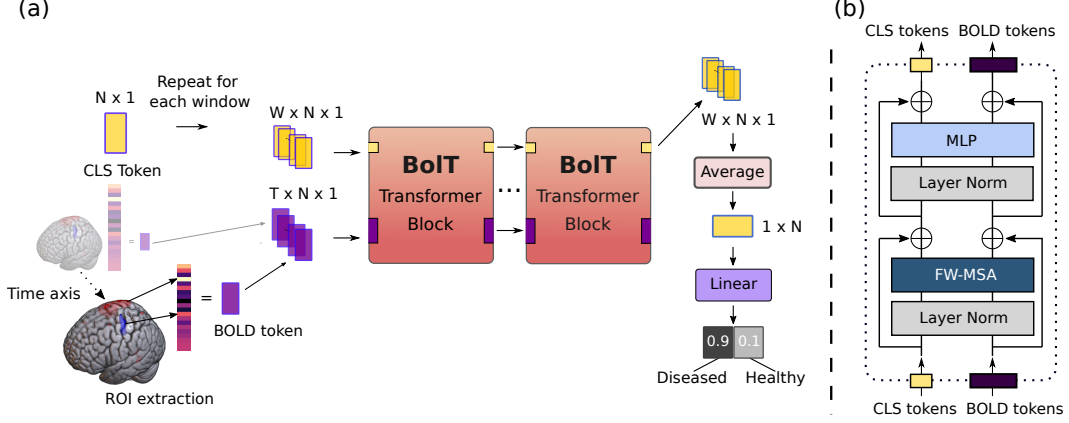


Figure 1: (a) Overview of BoIT. ROI time series are extracted from 4-D fMRI data to obtain a sequence of vectors, so-called BOLD tokens. We utilize an extra learnable "classification feature" called the *CLS* token for each time window. BOLD tokens for a given scan along with *CLS* tokens are provided as input the cascaded transformer blocks in BoIT. BoIT computes as output latent representation of the input tokens; only *CLS* tokens are used for the classification task at the output layer. (b) Inner architecture of the BoIT transformer block. Unlike vanilla transformers, The BoIT transformer is equipped with our novel fused windowed multi-head self-attention (FW-MSA) mechanism to effectively capture both local and global spatio-temporal representations.

3.1.1 Fused window attention

FW-MSA layers enable cross-window interactions by attention calculation between base tokens in a given window and fringe tokens from neighboring windows. To do this, FW-MSA first splits the entire collection of BOLD tokens $b \in R^{T \times N}$ into $F = (T - W)/s + 1$ windows of size W and stride s . A given window contains W base tokens within its body, and L fringe tokens on either side of the window are considered. While processing the i -th window, FW-MSA receives as input a collection of *CLS* ($CLS_i \in R^N$) and BOLD ($b_i \in R^{(W+2L) \times N}$) tokens. Let $Q_i \in R^{(1+W) \times N}$ denote queries for base tokens, and $K_i \in R^{(1+W+2L) \times N}$ and $V_i \in R^{(1+W+2L) \times N}$ respectively denote keys and value for the union of base and fringe tokens. Assuming f_q, f_k and f_v are learnable linear projections, the query, key and value for i -th window are:

$$Q_i = f_q(\{CLS_i, b^{(i*s)}, \dots, b^{(i*s+W-1)}\}), \quad K_i = f_k(\{CLS_i, b^{(i*s-L)}, \dots, b^{(i*s+W+L-1)}\}) \quad (1)$$

$$V_i = f_v(\{CLS_i, b^{(i*s-L)}, \dots, b^{(i*s+W+L-1)}\}) \quad (2)$$

To leverage information in the temporal ordering of BOLD tokens, we incorporate a relative position bias in attention calculations [35, 52]:

$$Attention(Q_i, K_i, V_i) = Softmax\left(\frac{Q_i K_i^T}{\sqrt{d}} + B\right) V_i, \quad (3)$$

where $B \in R^{(1+W) \times (1+W+2L)}$ is a learnable positional bias matrix and d is the feature dimensionality of the attention head. B expresses the relative position of the base BOLD tokens and the *CLS* token from all tokens in the receptive field including base and fringe tokens and the *CLS* token. For BOLD tokens, B parametrizes the potential range $[-W - L + 1, W + L - 1]$ of relative distances among tokens in difference positions of the receptive field. For the *CLS* token, it instead serves to distinguish the *CLS* token from the BOLD tokens.

3.1.2 Token fuser

Calculation of latent representations within temporal windows of fMRI data helps improve local precision and achieves linear scalability. Yet, BOLD signals do not only reflect brain dynamics at short time scale but they also contain information regarding interactions at broader time scales [27]. To capture global interactions across separate time windows, BoIT leverages a unique token fuser that

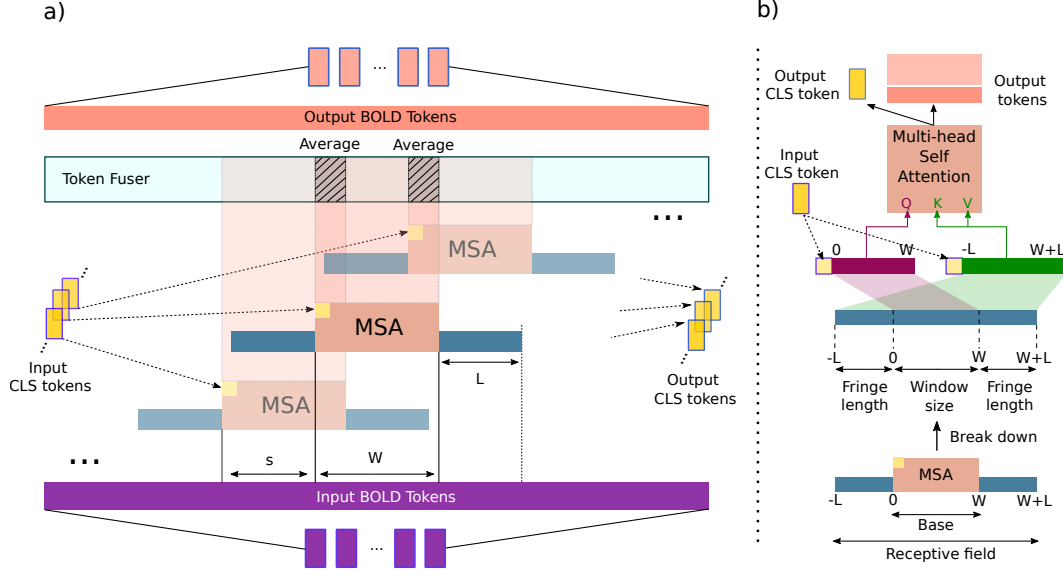


Figure 2: (a) Overview of the proposed fused window multi-head self-attention (FW-MSA) layer. Input BOLD tokens are separated into an overlapping set of time windows. Each time window also receives a unique *CLS* token. Within-window interactions are captured via attention among base tokens, whereas across-window interactions are captured via attention between base and fringe tokens. For each BOLD token, attention-derived latent representations are then fused across the separate time windows it appears in. (b) Attention calculations within a window. Query to the MSA is a BOLD token from the window base, whereas key and value are BOLD tokens from the receptive field including the fringe region.

aggregates the latent representations of a given BOLD token encoded within multiple overlapping time windows. In turn, fusion of BOLD tokens enables exchange of information across separate time windows, while maintaining a fixed number of BOLD tokens across transformer blocks. In BoIT, an unweighted averaging operator was adopted for token fusion:

$$b^{(i)}[m] = \frac{1}{P} \sum_{p=0}^{P-1} b_p^{(i)}[m-1] \quad (4)$$

where $m \in \{0, 1, \dots, M-1\}$ is the index of the transformer block, p is the index of the time window among P windows that contain a particular token, $b_p^{(i)}[m-1]$ is the i -th input BOLD token, and $b^{(i)}[m]$ is the fused token. Following fusion, all tokens are forwarded to the MLP block.

3.1.3 Cross-window regularization

The first transformer block in BoIT receives as input a single *CLS* token shared across the time windows. The transformer encoders then compute a unique *CLS* token for each window based on the BOLD tokens within its receptive field. If the latent space of window-level representations captured by the *CLS* tokens are largely incompatible, model performance in downstream classification tasks can be compromised. Thus, to encourage high-level representations that are consistent across time windows, we introduce a novel cross-window regularization via an additional loss term:

$$L_{CWR} = \frac{1}{NF} \cdot \sum_{i=0}^{F-1} \|CLS_i[M-1] - \frac{1}{F} (\sum_{j=0}^{F-1} CLS_j[M-1])\|_2^2 \quad (5)$$

where $CLS_i[M-1]$ is the encoded *CLS* token for the i -th window at the output of the last transformer block (M^{th}). The regularization term in Eq. 5 penalized the deviation of individual *CLS*

Algorithm 1: Calculation of relevancy map

Input: $\{\{A_{0(0)}, \dots, A_{0(F-1)}\}, \dots, \{A_{M-1(0)}, \dots, A_{M-1(F-1)}\}\}$: Set of F individual-window attention maps from FW-MSA layers across M transformer blocks.

Output: $R[M]$: Relevancy map.

```
1  $R[0] = \mathbf{I}_{F+T}$  Initialize relevancy map as identity matrix
2 for  $m = 0 : M - 1$  do
3    $\bar{A}_G[m] = \mathbf{0}_{F+T}$  Initialize global attention map as zero matrix
4   for  $i = 0 : F - 1$  do
5      $\bar{A}_{mi} \leftarrow E_h((\nabla A_{mi} \odot A_{mi})^+)$  Gradient-weighted attention map based on Eq. 6
6      $t' \leftarrow F + i * s$ 
7      $\bar{A}_G[m](i, i) \leftarrow \bar{A}_{mi}(0, 0)$  CLS to CLS attention
8      $\bar{A}_G[m](i, t' : t' + W') \leftarrow \bar{A}_{mi}(0, 1 : )$  CLS to BOLD attention
9      $\bar{A}_G[m](t' : t' + W, i) \leftarrow \bar{A}_{mi}(1 : , 0)$  BOLD to CLS attention
10     $\bar{A}_G[m](t' : t' + W, t' : t' + W') \leftarrow \bar{A}_G[m](t' : t' + W, t' : t' + W') + \bar{A}_{mi}(1 : , 1 : )$ 
      BOLD to BOLD attention
11     $\bar{A}_G[m] \leftarrow \bar{A}_G[m] \oslash A_{norm}$  Normalize for repeated occurrence of token in multiple windows
       $R[m+1] \leftarrow R[m] + \bar{A}_G[m]R[m]$  Update relevancy map
12 return  $R[M]$ 
```

tokens from their mean across time windows. For visualization of the output tokens with and without cross-window regularization, see Figure 3 in the Appendix.

3.1.4 Explainability

To interpret the classification decisions rendered by BolT, we computed a relevancy map across BOLD tokens in the input fMRI time series. Inspired by a recent explanatory method for proposed vanilla MSA layers [7], we computed relevancy scores for each token within the map based on gradient weighted attention maps at each layer. However, since we leveraged fused window attention over overlapping windows, a modified procedure was devised to calculate attention maps in BolT (Alg. 1). Given a total of F windows and T BOLD tokens, the relevancy map was initialized as an identity matrix in $R^{(F+T) \times (F+T)}$, implying that each BOLD or CLS is initially self-relevant. Afterwards, gradient-weighted individual-window attention maps were calculated for each transformer block and for each time window in the corresponding FW-MSA layer:

$$\bar{A}_{mi} = E_h((\nabla A_{mi} \odot A_{mi})^+) \quad (6)$$

In Eq. 6, $A_{mi} \in R^{(1+W) \times (1+W+2L)}$ is the attention map at the m^{th} block and i^{th} window, and ∇A_{mi} is its gradient, E_h denotes the averaging operator across attention heads, \odot is the Hadamard product, and $^+$ denotes rectification. To form the global attention map across the entire time series ($\bar{A}_G[m] \in R^{(F+T) \times (F+T)}$), individual-window attention maps were aggregated. Projections of tokens that appeared in multiple windows were averaged across windows. Assuming that $W' = W + 2L$, $t' = F + i * s$ and \bar{A}_{mi} is the i -th window's attention map, the projection is expressed as:

$$\bar{A}_G[m](i, i) = \bar{A}_{mi}(0, 0) \quad (7)$$

$$\bar{A}_G[m](i, t' : t' + W') = \bar{A}_{mi}(0, 1 :) \quad (8)$$

$$\bar{A}_G[m](t' : t' + W, i) = \bar{A}_{mi}(1 : , 0) \quad (9)$$

$$\bar{A}_G[m](t' : t' + W, t' : t' + W') = \bar{A}_{mi}(1 : , 1 :) \quad (10)$$

$$\bar{A}_G[m] = \bar{A}_G[m] \oslash A_{norm} \quad (11)$$

Here, Eq. (7) denotes the self-attention term for CLS_i , Eq. 8 denotes attention between CLS_i and BOLD tokens within the receptive field of the i -th window, Eq. 9 denotes attention between base BOLD tokens and the CLS_i token, and Eq. 10 denotes attention between based and fringe BOLD tokens. Note that Eqs. 7-10 follow NumPy's convention for array indexing starting at zero, and $(a : b + 1)$ corresponds to taking elements from index a to b [24]. Meanwhile, \oslash denotes Hadamard

Table 1: Comparison of BolT with competing models on HCP dataset.

Model	HCP-Rest		HCP-Task	Input Type
	Acc (%)	AUROC (%)	Acc (%)	
BolT	91.85 \pm 1.87	97.19 \pm 0.65	99.54 \pm 0.16	Raw
R-TFF [37]	86.54 \pm 4.46	94.18 \pm 2.27	99.43 \pm 0.17	Raw
R-BAnD [38]	82.88 \pm 1.72	91.84 \pm 1.40	99.35 \pm 0.19	Raw
LSTM [17]	80.96 \pm 0.84	90.19 \pm 1.49	98.47 \pm 0.31	Raw
STAGIN [31]	82.98 \pm 2.39	89.63 \pm 1.89	99.06 \pm 0.27	Raw + dFC
BrainGNN [34]	74.84 \pm 2.95	82.25 \pm 3.16	90.96 \pm 0.50	sFC
BrainNetCNN [29]	83.44 \pm 1.24	90.96 \pm 0.67	97.15 \pm 0.34	sFC
SVM [1]	75.84 \pm 2.47	84.97 \pm 2.19	92.61 \pm 0.68	sFC

division in Eq. 11 used in a normalization operation to account for repeated occurrence of a token across multiple overlapping time windows. The normalized global attention map at the m^{th} block was then used to update the relevancy map and pass it onto the next transformer block:

$$R[m+1] = R[m] + \bar{A}_G[m]R[m] \quad (12)$$

Following the calculation of the relevancy map at the final FW-MSA layer, importance weights for input BOLD tokens w_{imp} were finally derived as:

$$w_{imp} = \frac{1}{F} \sum_{i=0}^{F-1} R[M](i, F :) \quad (13)$$

Importance weight of a BOLD token for the classification task was taken as the across-window average of relevancy scores between the CLS tokens and the given BOLD token.

3.2 Datasets

Demonstrations were performed on fMRI data from the publicly available HCP S1200 release¹ [50] and Autism Brain Imaging Data Exchange (ABIDE) I dataset² [15], collected from anonymous voluntary participants with informed consent. For HCP S1200, pre-processed fMRI data from resting-state (HCP-Rest) and task-based (HCP-Task) scans were analyzed. For HCP-Rest, the first resting-state run among four sessions were used, and incomplete scans with $T < 1200$ were excluded from the analysis. HCP-Rest comprised a total of 1093 scans from 594 female and 499 male subjects. A gender prediction task was performed on HCP-Rest data. HCP-Task comprised a total of 7450 scans from 594 female and 499 male subjects, who performed seven different tasks in separate runs: emotion, relational, gambling, language, social, motor, working memory. Cognitive task detection was performed on HCP-Task data. For ABIDE I, pre-processed fMRI data from resting-state scans were analyzed as released by the Pre-processed Connectomes Project³ [12] without global signal regression and band-pass filtering. Specifically, data processed with the Configurable Pipeline for the Analysis of Connectomes [13] (C-PAC) was used. Low-quality scans that did not pass quality checks from all raters, and scans with zero signal throughout the scan in one or more atlas ROIs were excluded from analysis. ABIDE I comprised a total of 672 scans from 311 patients with Autism Spectrum Disorder (ASD) and 351 healthy controls, recruited from 16 different imaging sites. More detailed information regarding the analyzed datasets can be found in the Appendix Section C.

3.3 Experimental settings

Experiments were conducted in the PyTorch framework on a workstation equipped with an AMD EPYC 7302P CPU and a single NVIDIA GeForce RTX 3090 GPU. Model training was performed to minimize the following loss: $L = L_{CE} + \lambda \cdot L_{CWR}$ where L_{CE} is the cross-entropy loss and λ is the

¹<https://db.humanconnectome.org>, available under the condition to agree to the Open Access Data Use Terms

²https://fcon_1000.projects.nitrc.org/indi/abide/, available under CC BY-NC-SA 3.0 license

³<http://preprocessed-connectomes-project.org/abide/>

Table 2: Comparison of BolT with competing models on ABIDE-I dataset.

Model	ABIDE-I		Input Type
	Acc (%)	AUROC (%)	
BolT	69.36 \pm 5.16	75.99 \pm 5.55	Raw
R-TFF [37]	64.68 \pm 6.46	73.49 \pm 5.50	Raw
R-BAnD [38]	66.59 \pm 5.83	73.41 \pm 6.56	Raw
LSTM [17]	64.56 \pm 5.53	69.99 \pm 5.35	Raw
STAGIN [31]	59.13 \pm 4.97	63.92 \pm 6.11	Raw + dFC
BrainGNN [34]	60.64 \pm 4.38	64.94 \pm 4.53	sFC
BrainNetCNN [29]	67.16 \pm 5.34	73.52 \pm 5.44	sFC
SVM [1]	64.66 \pm 5.70	70.63 \pm 5.95	sFC

regularization coefficient for the CWR loss in Eq. 5. Cross-validation was performed on HCP-Rest for hyperparameter selection (Appendix A, Table 4), and the selected set of parameters were observed to yield near-optimal performance across all tasks. Accordingly, we prescribed $\lambda=1$, window size of $W=20$, stride coefficient of $\alpha=0.4$, fringe coefficient of $\beta=2$, and the number of attention heads as 36. A dropout rate of 0.1 was used in both FW-MSA and MLP layers. A one-cycle scheduler was used during model training, where learning rate was gradually increased from $2e-4$ to $5e-4$ in the first 30% of training iterations and then gradually decreased to $2e-5$. The minibatch size was 16 for HCP-Task and HCP-Rest, and 32 for ABIDE I. Model training was continued for 20 epochs.

Classification performance in gender prediction, task prediction and disease detections tasks was examined. The proposed model was compared against previous state-of-the-art transformer models (TFF [37], BAnD [38]), RNN models (LSTM [17]), GNN models (STAGIN [31], BrainGNN [34]), CNN models (BrainNetCNN [29]), along with a traditional SVM baseline with RBF kernel [1]. TFF and BAnD were observed to suffer from poor learning when these models were trained from scratch with voxel-level inputs as originally proposed. To improve performance, 3D CNN modules in TFF and BAnD were excluded and the remaining transformer blocks were provided as input ROI-level inputs. A linear projection layer was included to match the dimensionality of hidden representations to that expected by the original transformer blocks. These improved variants are referred to as R-TFF and R-BAnD. Competing models were implemented using the original toolboxes provided by the respective authors, and the originally recommended hyperparameters [17, 29, 34, 31, 38, 37]. In cases where poor performance was observed during training, the number of epochs and minibatch size were optimized for competing methods via cross-validation.

For HCP-Rest and HCP-Task, evaluations were performed via five-fold cross-validation with a single random-seed initialization for HCP-Rest and HCP-Task. For the intrinsically noisier ABIDE I, evaluations were performed via ten-fold cross-validation averaged across five random-seed initializations. To prevent bias, all competing models were trained and tested on identical data splits. During training, as proposed in [31], the fMRI time series for each scan from each subject were randomly cropped to a fixed length (of duration 600 for HCP-Rest, 150 for HCP-Task, and 60 for ABIDE-I). ROI s were defined according to the Schaefer atlas [44] with 400 regions labeled across seven intrinsic connectivity networks (ICNs).

4 Results

We first demonstrated the performance of BolT in gender prediction on HCP-Rest and cognitive task prediction on HCP-Task (Table 1). BolT outperforms other state-of-the-art transformer, RNN, GNN and CNN models along with a traditional baseline. For gender prediction, BolT maintains 91.85% accuracy with 5.31% improvement over the second-best method. While all methods show solid performance in cognitive task prediction, BolT again achieves the highest performance of 99.54%. HCP S1200 release contains high-resolution data (2 mm isotropic) collected at a single site with long run times (1200 samples for HCP-Rest). To examine performance on relatively noisier dataset collected at multiple sites, we also demonstrated BolT in disease detection on ABIDE-I (Table 2). BolT achieves the highest ASD detection accuracy of 69.36%, with 2.20% improvement over the second-best method. Taken together, these results demonstrate that BolT enables generalizable performance improvements over prior fMRI analysis models.

To interpret the spatio-temporal patterns of brain activation that contribute to the classification decisions, we employed the explanatory method described in Section 3.1.4 to calculate relevancy maps across input BOLD tokens within the fMRI time series. We first interrogated the task prediction model trained on HCP-Task. The relevancy maps for each cognitive task are given as averaged across subjects in Figure 4 in Appendix A. Overall, landmark time points that the model captures closely align with transitions in the temporal structure of task variables following an offset due to hemodynamic delay. For instance, in the working memory task, BolT focuses on time periods of target maintenance following target appearance during which abrupt changes in brain activation are observed. These results are at large consistency with recent studies reporting a tight correlation between functional connectivity and spontaneous increases/decreases in the BOLD signal [46]. Therefore, our findings suggest that sudden changes in activation patterns predominantly reflect brain state alterations driven by the timing of task variables, and that BolT successfully captures these state alterations during the fMRI scan to successfully classify cognitive task without any supervision regarding the temporal task structure.

Next, we leveraged the landmark time points relevant to BolT to identify brain regions critical for the classification tasks. For this purpose, we trained a logistic regression model to map activations recorded in landmark time points onto the associated output class as illustrated in Figure 5 in Appendix A. The top five most relevant BOLD tokens were used in each subject, under the assumption that these tokens contain sufficient discriminative information for the classification task as evidenced by recent fMRI reports [47, 46]. Accuracy of the logistic regression model for the classification tasks in HCP-Rest, HCP-Task; and ABIDE-I are listed in Table 3 in Appendix A. The logistic regression model based on relevant tokens significantly outperforms a logistic regression model based on random tokens (which yields nearly chance-level performance). For further validation of both the logistic regression model and the relevancy maps, multiple sets of five tokens were selected with varying degrees of relevance to build the logistic regression model as shown in Figure 6 in Appendix A. In all datasets, classification accuracy elevates near-monotonically with increasing levels of token relevance. This results indicates that the relevance scores closely reflect the contribution of individual BOLD tokens to the classification decisions, and BolT’s attention maps carry idiosyncratic information that help identify landmark BOLD tokens.

Following validation of the logistic regression model, we visualized the important ROIs in BOLD tokens that are assigned higher weights in the regression model to infer the spatial distribution of brain regions that are influential in task performance. Results are shown for gender classification in Figure 5, for task classification in Figure 7, and for ASD classification in Figure 8 in Appendix A. For gender classification, elevated BOLD signals in ROIs across the attention and somatosensory networks are associated with male subjects, and those in ROIs across prefrontal/frontal cortices and default mode network (DMN) are associated with female subjects. The gender-specific distribution of task-relevant brain regions are highly consistent with previous fMRI studies [42, 19], which report stronger functional connectivity across sensorimotor cortices in males and across DMN in females. Our analyses further reveal that important ROIs are presented across visual networks in both male and female subjects. This finding is aligned with a recent report suggesting that regions in visual cortex carry significant information that contribute to gender classification from fMRI data [31]. Meanwhile, during ASD classification, we find elevated BOLD signals in healthy controls within ROIs across the frontal-parietal network (FPN), which is hypothesized to be involved in mediating goal-oriented, cognitively demanding behavior [49]. In contrast, ASD patients manifested elevated BOLD signals in ROIs across DMN. The DMN is commonly implicated in ASD [5, 1], and recent studies report characteristic over-activation in DMN along with response inhibition in FPN in ASD populations [11, 48]. Taken together, these results strongly indicate that BolT is a powerful architecture for capturing task-relevant spatio-temporal patterns of brain activation in both normal and disease states.

Acknowledgements

This study was supported in part by a TUBITAK BİDEB scholarship awarded to Hasan Atakan Bedel and Onat Dalmaz, and by TUBITAK ARDEB 2021 scholarship awarded to Hasan Atakan Bedel, and by TUBA GEBİP 2015 and BAGEP 2017 fellowships awarded to Tolga Çukur.

References

- [1] Alexandre Abraham, Michael P Milham, Adriana Di Martino, R Cameron Craddock, Dimitris Samaras, Bertrand Thirion, and Gael Varoquaux. Deriving reproducible biomarkers from multi-site resting-state data: An autism-based example. *NeuroImage*, 147:736–745, 2017.
- [2] Jeffrey S Anderson, Jared A Nielsen, Michael A Ferguson, Melissa C Burbach, Elizabeth T Cox, Li Dai, Guido Gerig, Jamie O Edgin, and Julie R Korenberg. Abnormal brain synchrony in down syndrome. *NeuroImage: Clinical*, 2:703–715, 2013.
- [3] Salim Arslan, Sofia Ira Ktena, Ben Glocker, and Daniel Rueckert. Graph saliency maps through spectral convolutional networks: Application to sex classification with brain connectivity. In *Graphs in biomedical image analysis and integrating medical imaging and non-imaging modalities*, pages 3–13. Springer, 2018.
- [4] Tom Brown, Benjamin Mann, Nick Ryder, Melanie Subbiah, Jared D Kaplan, Prafulla Dhariwal, Arvind Neelakantan, Pranav Shyam, Girish Sastry, Amanda Askell, et al. Language models are few-shot learners. *Advances in neural information processing systems*, 33:1877–1901, 2020.
- [5] Randy L Buckner, Jessica R Andrews-Hanna, and Daniel L Schacter. The brain’s default network: anatomy, function, and relevance to disease. *Annals of the new York Academy of Sciences*, 1124(1):1–38, 2008.
- [6] Vince D Calhoun, Jing Sui, Kent Kiehl, Jessica A Turner, Elena A Allen, and Godfrey Pearlson. Exploring the psychosis functional connectome: aberrant intrinsic networks in schizophrenia and bipolar disorder. *Frontiers in psychiatry*, 2:75, 2012.
- [7] Hila Chefer, Shir Gur, and Lior Wolf. Generic attention-model explainability for interpreting bi-modal and encoder-decoder transformers. In *Proceedings of the IEEE/CVF International Conference on Computer Vision*, pages 397–406, 2021.
- [8] Gang Chen, B Douglas Ward, Chunming Xie, Wenjun Li, Zhilin Wu, Jennifer L Jones, Malgorzata Franczak, Piero Antuono, and Shi-Jiang Li. Classification of alzheimer disease, mild cognitive impairment, and normal cognitive status with large-scale network analysis based on resting-state functional mr imaging. *Radiology*, 259(1):213–221, 2011.
- [9] Gang Chen, B Douglas Ward, Chunming Xie, Wenjun Li, Zhilin Wu, Jennifer L Jones, Malgorzata Franczak, Piero Antuono, and Shi-Jiang Li. Classification of alzheimer disease, mild cognitive impairment, and normal cognitive status with large-scale network analysis based on resting-state functional mr imaging. *Radiology*, 259(1):213–221, 2011.
- [10] Xiaobo Chen, Han Zhang, Lichi Zhang, Celina Shen, Seong-Whan Lee, and Dinggang Shen. Extraction of dynamic functional connectivity from brain grey matter and white matter for mci classification. *Human brain mapping*, 38(10):5019–5034, 2017.
- [11] Ya-Yun Chen, Mirko Uljarevic, Joshua Neal, Steven Greening, Hyungwook Yim, and Tae-Ho Lee. Excessive functional coupling with less variability between salience and default-mode networks in autism spectrum disorder. *Biological Psychiatry: Cognitive Neuroscience and Neuroimaging*, 2021.
- [12] Cameron Craddock, Yassine Benhajali, Carlton Chu, Francois Chouinard, Alan Evans, András Jakab, Budhachandra Singh Khundrakpam, John David Lewis, Qingyang Li, Michael Milham, et al. The neuro bureau preprocessing initiative: open sharing of preprocessed neuroimaging data and derivatives. *Frontiers in Neuroinformatics*, 7, 2013.
- [13] Cameron Craddock, Sharad Sikka, Brian Cheung, Ranjeet Khanuja, Satrajit S Ghosh, Chaogan Yan, Qingyang Li, Daniel Lurie, Joshua Vogelstein, Randal Burns, et al. Towards automated analysis of connectomes: The configurable pipeline for the analysis of connectomes (c-pac). *Front Neuroinform*, 42:10–3389, 2013.
- [14] Jacob Devlin, Ming-Wei Chang, Kenton Lee, and Kristina Toutanova. Bert: Pre-training of deep bidirectional transformers for language understanding. *arXiv preprint arXiv:1810.04805*, 2018.

- [15] Adriana Di Martino, Chao-Gan Yan, Qingyang Li, Erin Denio, Francisco X Castellanos, Kaat Alaerts, Jeffrey S Anderson, Michal Assaf, Susan Y Bookheimer, Mirella Dapretto, et al. The autism brain imaging data exchange: towards a large-scale evaluation of the intrinsic brain architecture in autism. *Molecular psychiatry*, 19(6):659–667, 2014.
- [16] Alexey Dosovitskiy, Lucas Beyer, Alexander Kolesnikov, Dirk Weissenborn, Xiaohua Zhai, Thomas Unterthiner, Mostafa Dehghani, Matthias Minderer, Georg Heigold, Sylvain Gelly, et al. An image is worth 16x16 words: Transformers for image recognition at scale. *arXiv preprint arXiv:2010.11929*, 2020.
- [17] Nisha C Dvornek, Pamela Ventola, Kevin A Pelphrey, and James S Duncan. Identifying autism from resting-state fmri using long short-term memory networks. In *International Workshop on Machine Learning in Medical Imaging*, pages 362–370. Springer, 2017.
- [18] Yong Fan, Hengyi Rao, Hallam Hurt, Joan Giannetta, Marc Korczykowski, David Shera, Brian B Avants, James C Gee, Jiongjiong Wang, and Dinggang Shen. Multivariate examination of brain abnormality using both structural and functional mri. *NeuroImage*, 36(4):1189–1199, 2007.
- [19] Massimo Filippi, Paola Valsasina, Paolo Misci, Andrea Falini, Giancarlo Comi, and Maria A Rocca. The organization of intrinsic brain activity differs between genders: A resting-state fmri study in a large cohort of young healthy subjects. *Human brain mapping*, 34(6):1330–1343, 2013.
- [20] Karl J Friston. Functional and effective connectivity in neuroimaging: a synthesis. *Human brain mapping*, 2(1-2):56–78, 1994.
- [21] Soham Gadgil, Qingyu Zhao, Adolf Pfefferbaum, Edith V Sullivan, Ehsan Adeli, and Kilian M Pohl. Spatio-temporal graph convolution for resting-state fmri analysis. In *International Conference on Medical Image Computing and Computer-Assisted Intervention*, pages 528–538. Springer, 2020.
- [22] Michael D Greicius, Ben Krasnow, Allan L Reiss, and Vinod Menon. Functional connectivity in the resting brain: a network analysis of the default mode hypothesis. *Proceedings of the National Academy of Sciences*, 100(1):253–258, 2003.
- [23] Michael D Greicius, Gaurav Srivastava, Allan L Reiss, and Vinod Menon. Default-mode network activity distinguishes alzheimer’s disease from healthy aging: evidence from functional mri. *Proceedings of the National Academy of Sciences*, 101(13):4637–4642, 2004.
- [24] Charles R Harris, K Jarrod Millman, Stéfan J Van Der Walt, Ralf Gommers, Pauli Virtanen, David Cournapeau, Eric Wieser, Julian Taylor, Sebastian Berg, Nathaniel J Smith, et al. Array programming with numpy. *Nature*, 585(7825):357–362, 2020.
- [25] Kaiming He, Xinlei Chen, Saining Xie, Yanghao Li, Piotr Dollár, and Ross Girshick. Masked autoencoders are scalable vision learners. *arXiv preprint arXiv:2111.06377*, 2021.
- [26] Elizabeth MC Hillman. Coupling mechanism and significance of the bold signal: a status report. *Annual review of neuroscience*, 37:161–181, 2014.
- [27] R Matthew Hutchison, Thilo Womelsdorf, Elena A Allen, Peter A Bandettini, Vince D Calhoun, Maurizio Corbetta, Stefania Della Penna, Jeff H Duyn, Gary H Glover, Javier Gonzalez-Castillo, et al. Dynamic functional connectivity: promise, issues, and interpretations. *Neuroimage*, 80: 360–378, 2013.
- [28] Aya Abdelsalam Ismail, Mohamed Gunady, Luiz Pessoa, Hector Corrada Bravo, and Soheil Feizi. Input-cell attention reduces vanishing saliency of recurrent neural networks. *Advances in Neural Information Processing Systems*, 32, 2019.
- [29] Jeremy Kawahara, Colin J Brown, Steven P Miller, Brian G Booth, Vann Chau, Ruth E Grunau, Jill G Zwicker, and Ghassan Hamarneh. Brainnetcn: Convolutional neural networks for brain networks; towards predicting neurodevelopment. *NeuroImage*, 146:1038–1049, 2017.
- [30] Byung-Hoon Kim and Jong Chul Ye. Understanding graph isomorphism network for rs-fmri functional connectivity analysis. *Frontiers in neuroscience*, page 630, 2020.

- [31] Byung-Hoon Kim, Jong Chul Ye, and Jae-Jin Kim. Learning dynamic graph representation of brain connectome with spatio-temporal attention. *Advances in Neural Information Processing Systems*, 34, 2021.
- [32] Sofia Ira Ktena, Sarah Parisot, Enzo Ferrante, Martin Rajchl, Matthew Lee, Ben Glocker, and Daniel Rueckert. Metric learning with spectral graph convolutions on brain connectivity networks. *NeuroImage*, 169:431–442, 2018.
- [33] Megan H Lee, Christopher D Smyser, and Joshua S Shimony. Resting-state fmri: a review of methods and clinical applications. *American Journal of neuroradiology*, 34(10):1866–1872, 2013.
- [34] Xiaoxiao Li, Yuan Zhou, Nicha Dvornek, Muhan Zhang, Siyuan Gao, Juntang Zhuang, Dustin Scheinost, Lawrence H Staib, Pamela Ventola, and James S Duncan. Braingnn: Interpretable brain graph neural network for fmri analysis. *Medical Image Analysis*, 74:102233, 2021.
- [35] Ze Liu, Yutong Lin, Yue Cao, Han Hu, Yixuan Wei, Zheng Zhang, Stephen Lin, and Baining Guo. Swin transformer: Hierarchical vision transformer using shifted windows. In *Proceedings of the IEEE/CVF International Conference on Computer Vision*, pages 10012–10022, 2021.
- [36] Zilu Ma, Qingqing Zhang, Wenyu Tu, and Nanyin Zhang. Gaining insight into the neural basis of resting-state fmri signal. *Neuroimage*, 250:118960, 2022.
- [37] Itzik Malkiel, Gony Rosenman, Lior Wolf, and Talma Hendler. Pre-training and fine-tuning transformers for fmri prediction tasks. *arXiv preprint arXiv:2112.05761*, 2021.
- [38] Sam Nguyen, Brenda Ng, Alan D Kaplan, and Priyadip Ray. Attend and decode: 4d fmri task state decoding using attention models. In *Machine Learning for Health*, pages 267–279. PMLR, 2020.
- [39] Sarah Parisot, Sofia Ira Ktena, Enzo Ferrante, Matthew Lee, Ricardo Guererro Moreno, Ben Glocker, and Daniel Rueckert. Spectral graph convolutions for population-based disease prediction. In *International conference on medical image computing and computer-assisted intervention*, pages 177–185. Springer, 2017.
- [40] Alec Radford, Jeffrey Wu, Rewon Child, David Luan, Dario Amodei, Ilya Sutskever, et al. Language models are unsupervised multitask learners. *OpenAI blog*, 1(8):9, 2019.
- [41] Jonas Richiardi, Markus Gschwind, Samanta Simioni, Jean-Marie Annoni, Beatrice Greco, Patric Hagmann, Myriam Schluep, Patrik Vuilleumier, and Dimitri Van De Ville. Classifying minimally disabled multiple sclerosis patients from resting state functional connectivity. *Neuroimage*, 62(3):2021–2033, 2012.
- [42] Stuart J Ritchie, Simon R Cox, Xueyi Shen, Michael V Lombardo, Lianne M Reus, Clara Alloza, Mathew A Harris, Helen L Alderson, Stuart Hunter, Emma Neilson, et al. Sex differences in the adult human brain: evidence from 5216 uk biobank participants. *Cerebral cortex*, 28(8):2959–2975, 2018.
- [43] Mikail Rubinov and Olaf Sporns. Complex network measures of brain connectivity: uses and interpretations. *Neuroimage*, 52(3):1059–1069, 2010.
- [44] Alexander Schaefer, Ru Kong, Evan M Gordon, Timothy O Laumann, Xi-Nian Zuo, Avram J Holmes, Simon B Eickhoff, and BT Thomas Yeo. Local-global parcellation of the human cerebral cortex from intrinsic functional connectivity mri. *Cerebral cortex*, 28(9):3095–3114, 2018.
- [45] Matthew J Singleton. Functional magnetic resonance imaging. *The Yale journal of biology and medicine*, 82(4):233, 2009.
- [46] Enzo Tagliazucchi, Pablo Balenzuela, Daniel Fraiman, Pedro Montoya, and Dante R Chialvo. Spontaneous bold event triggered averages for estimating functional connectivity at resting state. *Neuroscience letters*, 488(2):158–163, 2011.

- [47] Enzo Tagliazucchi, Pablo Balenzuela, Daniel Fraiman, and Dante R Chialvo. Criticality in large-scale brain fmri dynamics unveiled by a novel point process analysis. *Frontiers in physiology*, 3: 15, 2012.
- [48] Lucina Q Uddin. *Salience network of the human brain*. Academic press, 2016.
- [49] Lucina Q Uddin, BT Yeo, and R Nathan Spreng. Towards a universal taxonomy of macro-scale functional human brain networks. *Brain topography*, 32(6):926–942, 2019.
- [50] David C Van Essen, Stephen M Smith, Deanna M Barch, Timothy EJ Behrens, Essa Yacoub, Kamil Ugurbil, Wu-Minn HCP Consortium, et al. The wu-minn human connectome project: an overview. *Neuroimage*, 80:62–79, 2013.
- [51] Ashish Vaswani, Noam Shazeer, Niki Parmar, Jakob Uszkoreit, Llion Jones, Aidan N Gomez, Łukasz Kaiser, and Illia Polosukhin. Attention is all you need. *Advances in neural information processing systems*, 30, 2017.
- [52] Jianwei Yang, Chunyuan Li, Pengchuan Zhang, Xiyang Dai, Bin Xiao, Lu Yuan, and Jianfeng Gao. Focal self-attention for local-global interactions in vision transformers. *arXiv preprint arXiv:2107.00641*, 2021.
- [53] Xiaowei Yu, Lu Zhang, Lin Zhao, Yanjun Lyu, Tianming Liu, and Dajiang Zhu. Disentangling spatial-temporal functional brain networks via twin-transformers. *arXiv preprint arXiv:2204.09225*, 2022.

A Additional results

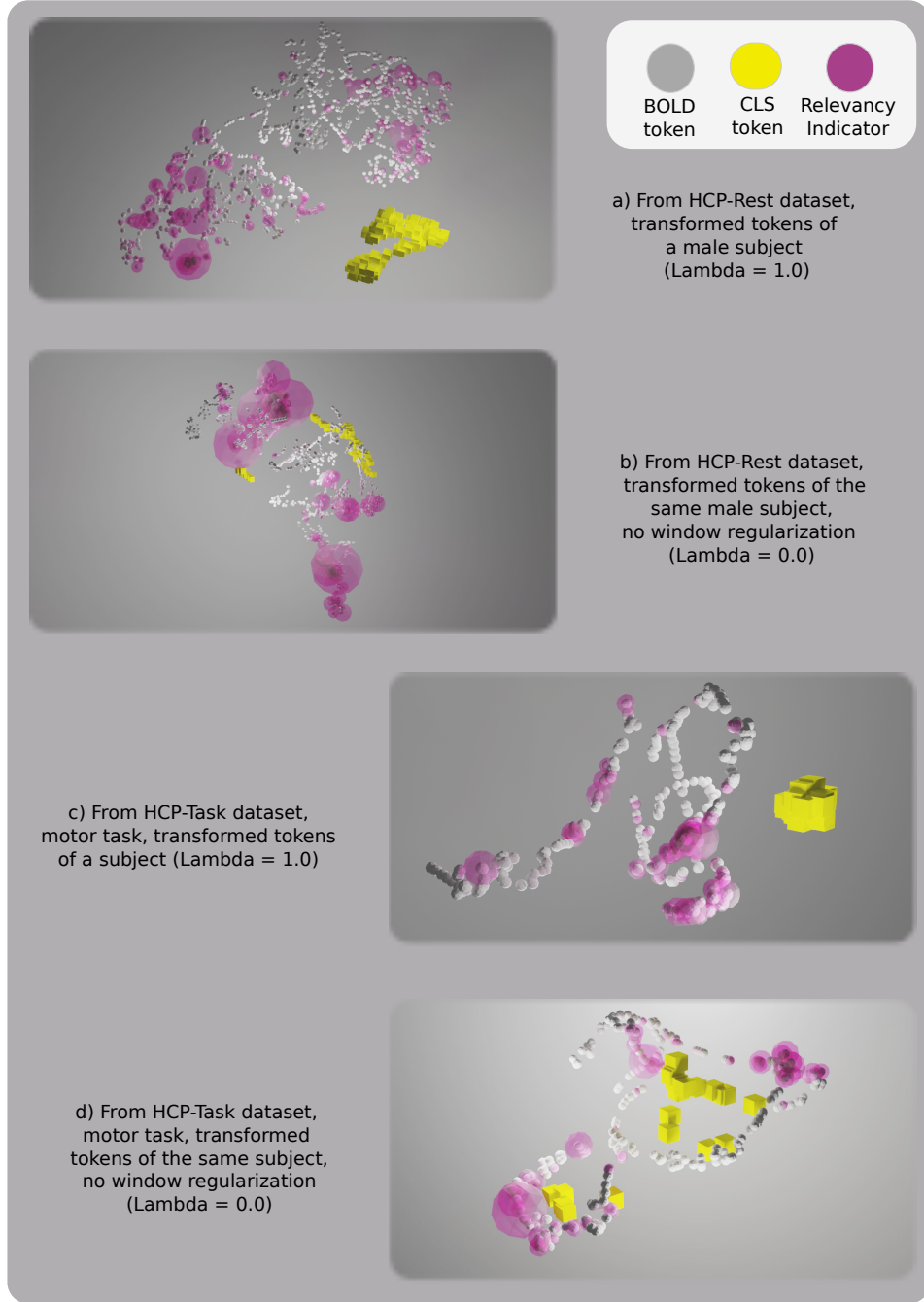


Figure 3: 3D t-SNE projections of latent representations for BOLD and *CLS* tokens extracted by BolT. Visualizations are provided for the cases with and without cross-window regularization. Cross-window regularization promotes *CLS* tokens to be spatially clustered, signaling the alignment of latent representations across windows. Regularization also improves alignment between relevant BOLD tokens and *CLS* tokens.

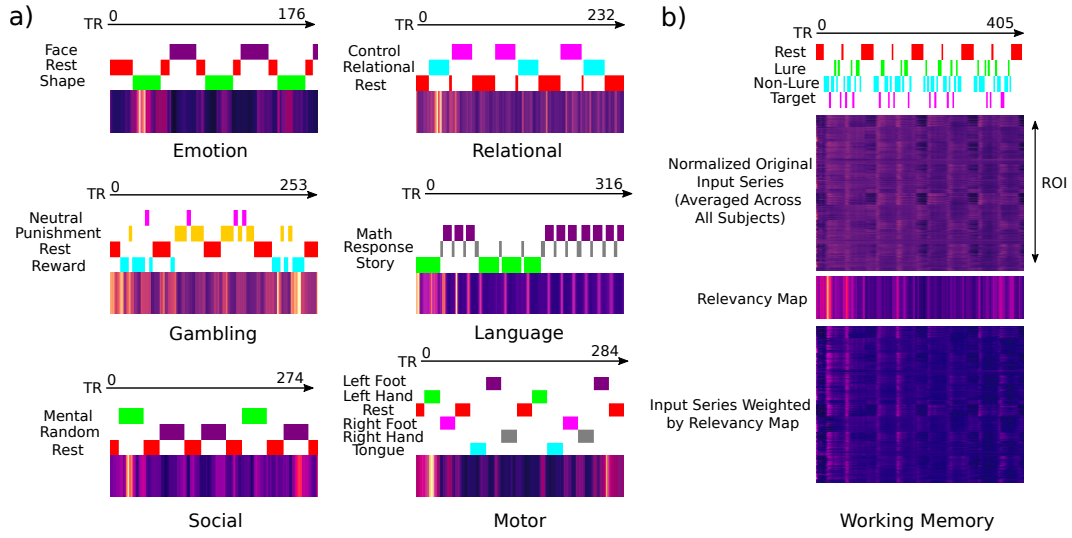


Figure 4: Relevancy maps for individual cognitive tasks in the HCP-Task dataset, averaged across subjects. (a) Relevancy maps for emotion, relational, gambling, language, social and motor tasks. Subtask annotations are shown to outline the temporal task structure. (b) Input fMRI time series averaged across all subjects for the working memory task. Critical ROIs and time points are highlighted by masking the input time series with the relevancy map.

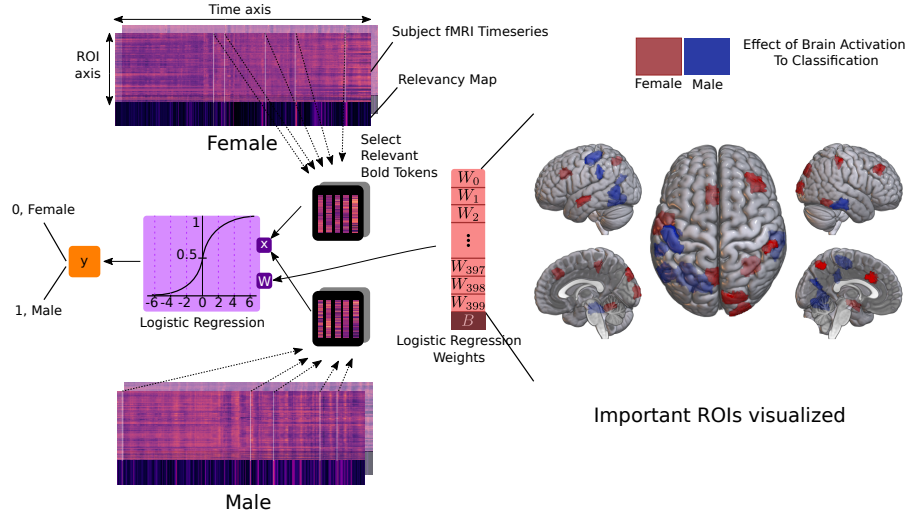


Figure 5: Landmark time points (i.e. BOLD tokens) selected by BolT are used to identify brain regions critical for gender classification in HCP-Rest data. A logistic regression model was trained to map the activations recorded in landmark time points onto the associated regression output class (i.e. female or male). The weights of the regression model reflect each ROI's contribution to the classification decision. For each class, the top 2 percent of most influential ROIs are visualized.

Table 3: Accuracy of logistic regression classifiers given as input most important tokens selected according to the relevancy map. Results are also listed for logistic regression on randomly selected tokens, BoIT, and SVM along with chance level.

Model	HCP-Rest	HCP-Task	ABIDE-I
	Acc (%)	Acc (%)	Acc (%)
Logistic Reg (Relevant Tokens)	71.36 ± 2.36	77.28 ± 5.67	60.30 ± 5.71
Logistic Reg (Random Tokens)	50.31 ± 1.23	15.46 ± 0.70	51.52 ± 5.44
Random Chance	50.00	14.28	50.00
BoIT	91.85 ± 1.87	99.54 ± 0.16	69.36 ± 5.16
SVM	75.84 ± 2.47	92.61 ± 0.68	64.66 ± 5.70

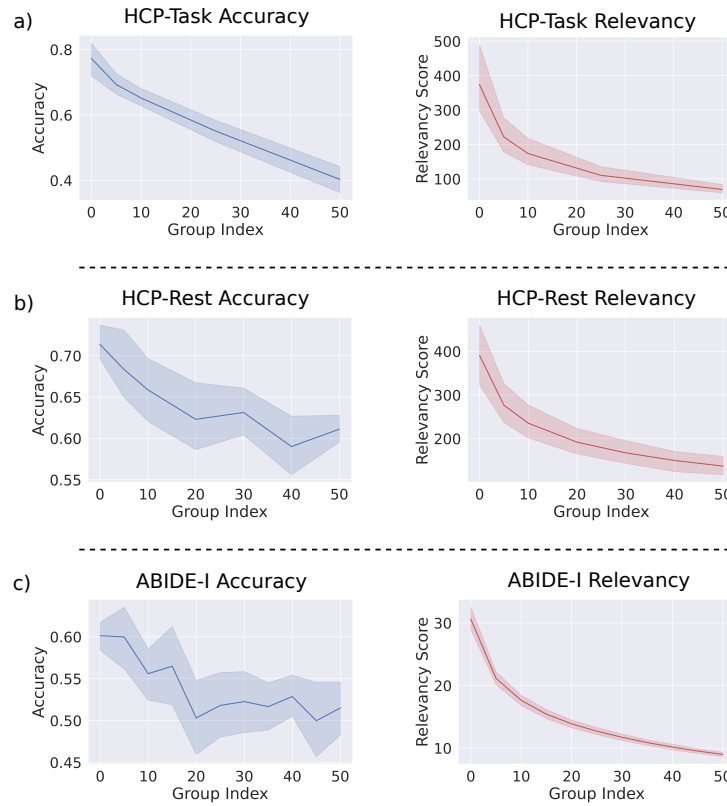


Figure 6: Accuracy of a logistic regression classifier trained on relevant tokens, and total relevancy scores of selected tokens were analyzed as a function of group index. Results are shown for (a) HCP-Task, (b) HCP-Rest, (c) ABIDE-I datasets. Tokens within the fMRI time series were ordered according to their relevancy scores. A group of five consecutive tokens in the ordered list were selected to build the classifier. Group index refers to the offset index within the ordered list after which the selection starts, so both relevancy scores and classification accuracy decrease with group index.

Table 3 lists percentage classification accuracy of the logistic regression model across the three datasets analyzed here. Selection of the BOLD tokens according to relevancy scores and accuracy of the logistic regression model were characterized as described in Section 4. For HCP-Rest and HCP-Task, regression results were reported via 5-fold cross-validation with a single seed; whereas

for ABIDE-I, results were reported via 10-fold cross-validation averaged across five seeds. In all cases, the logistic regression model on relevant tokens significantly outperforms a logistic regression model on randomly selected tokens. For HCP-Rest and ABIDE-I, the logistic regression model’s performance approaches that of an SVM classifier trained on FC features, illustrating the power of our proposed model to identify important landmarks in fMRI data.

To explore the interaction between token relevancy levels and model performance, logistic regression models were built on multiple sets of tokens with varying degrees of relevance as displayed in Figure 6. Here, the relevancy score is taken as the ratio of a token’s importance weight to the lowest weight across the time series. We find that there is a strong correlation between accuracy of the logistic regression model and the relevancy of the selected tokens, corroborating that BolT can sensitively identify landmark time points in fMRI data.

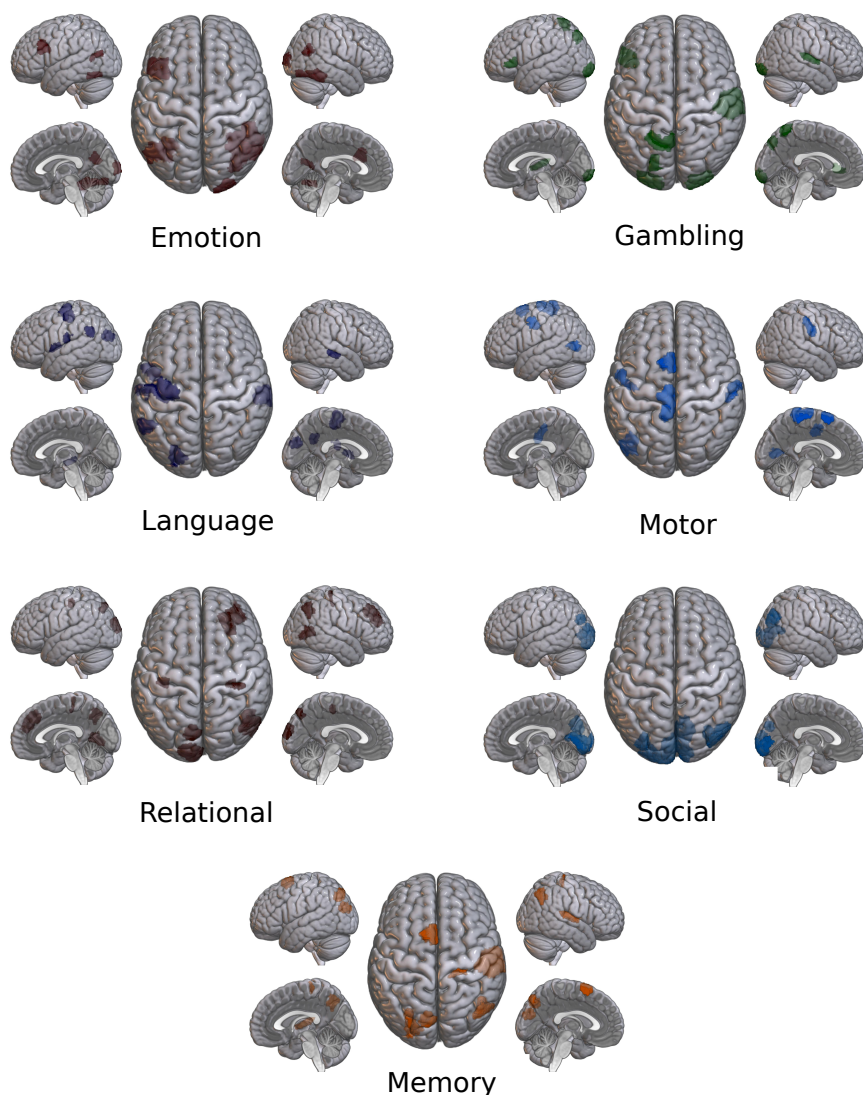


Figure 7: Critical ROIs for cognitive task prediction in the HCP-Task dataset. For each task, the top 2 percent of most influential ROIs are visualized. An increase in the BOLD activations of the influential ROIs implies the presence of the associated task.

Figure 7 illustrates the task-relevant ROIs identified for individual cognitive tasks within the HCP-Task dataset. Overall, for each individual task, canonical brain regions commonly implicated with that task are highlighted. For instance, sensorimotor regions are marked as important in the Motor task, and temporal regions are marked as important in the Language task.

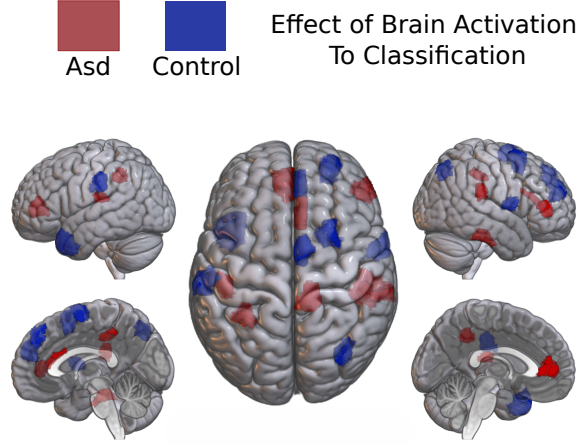


Figure 8: Critical ROIs for ASD detection in the ABIDE-I dataset. The top 2 percent of most influential ROIs are visualized for ASD patients and healthy controls. An increase in the BOLD activations of the red ROIs implies the presence of ASD, whereas an increase in activations of the blue ROIs implies a healthy control.

B Additional analyses

B.1 FW-MSA configuration

The FW-MSA layer in BolT has three key hyperparameters: window size, stride, and fringe length of the windows. Here we provide the heuristics employed to choose the stride and the fringe length. Given a desired window size W , we choose stride s and fringe length L as follows:

$$s = W\alpha, \quad L = m(W - s)\beta = m(1 - \alpha)W\beta \quad (14)$$

where $m \in \{0, 1, \dots, M - 1\}$ is the block number and stride coefficient (α) and fringe coefficient (β) are yet another parameters but in a relatively more strict range, $\alpha \in (0.0, 1.0)$ and $\beta \in \mathbb{Z}^+$. For the initial FW-MSA layer, the fringe length was initialized as 0 and progressively increased at each proceeding layer via multiplication with the number of fused tokens. For example, consider the setup on the HCP-Rest dataset with the hyperparameter choices described in Section 3.3. The window size, stride coefficient, and fringe coefficient was set to 20, 0.4, and 2, respectively. Consequently, the fringe length becomes 0, 24, 48, and 72, respectively, with the increasing layer number. This gives each window a receptive field of 20, 68, 116, and 164 BOLD tokens, respective to the growing layer number.

B.2 Hyperparameter settings

Table 4 summarizes the cross-validated search results for hyperparameter selection in BolT performed on the HCP-Rest gender prediction task. Three key hyperparameters of FW-MSA are listed (see Appendix B.1): window size, stride coefficient, and fringe coefficient. Beyond percentage accuracy and ROC metrics, we also reported the inference time of the model, and the total number of floating-point operations (FLOPs) in the FW-MSA layers for a single-subject fMRI scan of temporal length 1200. Note that a stride coefficient of 5/5 is equivalent to disabling token fusion and cross-window attention since there are no overlapping windows, and a fringe coefficient of 0 is equivalent to disabling cross-window attention as there are no fringe tokens to consider.

Table 4: BolT hyperparameters and performance metrics for HCP-Rest gender prediction.

Hyperparameter		Accuracy(%)	ROC(%)	Inference time(ms)	FLOPs (G)
Window Size	10	91.03 ± 1.23	97.06 ± 0.74	45.23 ± 2.58	40.37
	*20	91.85 ± 1.87	97.19 ± 0.65	34.72 ± 0.70	39.92
	80	91.12 ± 1.74	96.89 ± 0.73	30.63 ± 1.14	46.73
	200	90.30 ± 1.71	96.19 ± 0.92	48.46 ± 1.23	58.49
Stride Coeff.	1/5	89.38 ± 1.49	96.51 ± 1.03	65.40 ± 1.19	81.57
	*2/5	91.85 ± 1.87	97.19 ± 0.65	34.72 ± 0.70	39.92
	3/5	91.76 ± 1.01	97.16 ± 0.64	22.86 ± 3.04	26.13
	4/5	90.66 ± 1.18	97.19 ± 0.75	18.81 ± 1.26	19.10
	5/5	90.48 ± 1.92	96.67 ± 0.94	16.35 ± 0.31	15.14
Fringe Coeff.	0	90.93 ± 1.44	96.78 ± 1.02	25.35 ± 0.15	37.35
	1	91.58 ± 1.19	97.18 ± 0.58	28.58 ± 0.39	38.64
	*2	91.85 ± 1.87	97.19 ± 0.65	34.72 ± 0.70	39.92
	3	91.76 ± 1.39	97.15 ± 0.67	35.75 ± 1.95	41.21

* Asterisks indicate the settings reported during the main experiments.

B.3 Complexity analysis

The computational complexity of the proposed FW-MSA layer can be calculated by summing up the computation within each window. Each window has $W + 1$ number of queries and $W + 2L + 1$ number of keys and values. The complexity within the windows is $O(W^2 + WL)$. There are $(N - W)/s$ number of windows, which yields an overall complexity of $O(NW^2/s + NWL/s)$. Selecting s and L as suggested in Eq.14 results in an overall complexity of $O(NW^{\frac{(1+\beta(m)(1-\alpha))}{\alpha}})$, a linear function of the input length.

B.4 Ablation study

Several lines of ablation analyses were conducted to assess the value of each design component in BolT. Results of the ablation study performed on the HCP-Rest dataset for gender prediction are listed in Table 5. Model performance was examined to evaluate the contributions of *CLS* tokens (*CLS*), windowing of the fMRI time series in FW-MSA layers (Windowing), fusion of tokens across overlapping time windows (Fusion), cross-attention between base and fringe tokens in FW-MSA (Cross Attn.), and cross-window regularization of *CLS* tokens (CWR). To ablate *CLS*, aggregation of BOLD tokens via *CLS* was replaced with global average pooling of output BOLD tokens. To ablate Windowing, a single window that contained the entire fMRI time series was used. To ablate Fusion, the shift size between windows was set to ensure non-overlapping windows. To ablate Cross Attn., fringe length was set to 0 for each time window. To ablate CWR, the loss component for cross-window regularization was removed by setting $\lambda = 0$.

Table 5: Ablation study.

<i>CLS</i>	Windowing	Fusion	Cross Attn.	CWR	Accuracy (%)	ROC (%)
✗	✗	✗	✗	✗	86.09 ± 2.03	94.19 ± 0.89
✓	✗	✗	✗	✗	88.65 ± 1.33	95.54 ± 0.51
✓	✓	✗	✗	✗	89.56 ± 1.42	96.91 ± 0.79
✓	✓	✓	✗	✗	90.29 ± 1.41	96.82 ± 0.72
✓	✓	✓	✓	✗	90.75 ± 1.66	96.59 ± 0.79
✓	✓	✓	✓	✓	91.85 ± 1.87	97.19 ± 0.65

C Dataset details

Table 6 lists information for the HCP-Rest and HCP-Task datasets regarding the distribution of subjects across different tasks. In particular, the minimum and maximum age, gender, total number of scans, and scan length (T) are given.

Table 6: Description of the HCP dataset.

Dataset	Task Type	Age (year)		Gender		# Scans	T
		Min	Max	Female	Male		
HCP-Rest	Resting-state	22	36+	594	499	1093	1200
HCP-Task	Working Memory	22	36+	591	496	1087	405
	Social	22	36+	565	488	1053	274
	Relational	22	36+	558	485	1043	232
	Motor	22	36+	588	497	1085	284
	Language	22	36+	564	487	1051	316
	Gambling	22	36+	585	497	1082	253
	Emotion	22	36+	564	485	1049	176

Table 7 lists details of the ABIDE I dataset in terms of the distribution of subjects across sites. In particular, the selected number of subjects out of all available at each site, the number of ASD versus control subjects, the minimum and maximum age, gender, total number of scans, and range of scan length are given. The notation X/Y denotes that X out of Y available subjects were selected following quality checks.

Table 7: Descriptions of the ABIDE-I dataset.

Site	Diagnostic		Age(year)		Gender		# Scans	T
	ASD	Control	Min	Max	Male	Female		
CALTECH	0/5	0/10	-	-	0/10	0/5	0/15	-
CMU	4/6	3/5	22	33	6/7	1/4	7/11	202-236
KKI	11/12	14/21	8	13	20/24	5/9	25/33	124-152
LEUVEN_1	3/14	1/14	18	29	4/28	0/0	4/28	246
LEUVEN_2	4/12	7/16	12	17	7/21	4/7	11/28	246
MAX_MUN	15/19	24/27	7	58	37/42	2/4	39/46	116-196
NYU	50/74	67/98	6	31	98/136	19/36	117/172	176
OHSU	11/12	12/13	8	14	23/25	0/0	23/25	78
OLIN	14/14	13/14	10	24	22/23	5/5	27/28	206
PITT	23/24	25/26	9	35	41/43	7/7	48/50	196
SBL	4/12	8/14	26	42	12/26	0/0	12/26	196
SDSU	1/8	5/19	9	16	4/21	2/6	6/27	176
STANFORD	12/12	13/13	8	13	18/18	7/7	25/25	176-236
TRINITY	15/19	19/25	12	25	34/44	0/0	34/44	146
UCLA_1	36/37	24/27	8	18	52/55	8/9	60/64	116
UCLA_2	10/11	9/10	10	15	17/19	2/2	19/21	116
UM_1	31/34	52/52	8	19	58/61	25/25	83/86	296
UM_2	13/13	19/21	13	29	30/32	2/2	32/34	296
USM	35/43	19/24	9	50	54/67	0/0	54/67	232-236
YALE	19/22	17/19	7	18	23/25	13/16	36/41	196
Total	311/403	351/468	6	58	560/727	102/144	662/871	78-296